ADVANCED MATERIALS TECHNOLOGIES
www.advmattechnol.de

# An Underwater Cylinder-Enhanced Flag-Shaped Triboelectric Nanogenerator by Vortex-Induced Vibration for Low-Velocity Ocean Current Monitoring

*Zhenhan Zhuo, Peishuo Li, Shuang Li, Jicang Si,* Hengxu Du, Anglong Liu, Yu Zhang, Yongjiu Zou,* and Minyi Xu**

**Accurate ocean flow velocity monitoring is crucial for marine engineering and environmental sensing but faces challenges under low-flow conditions due to limited energy, power integration difficulties, and reduced sensor sensitivity. To overcome these, this work introduces a novel underwater cylinder-enhanced flag-shaped triboelectric nanogenerator (UCF-TENG). It utilizes vortex-induced vibrations (VIV) from an upstream bluff body for efficient flow detection. Based on a quantified Strouhal number relationship, the UCF-TENG provides a direct, linear mapping between flow velocity and output signal frequency. Experimental results demonstrate that the UCF-TENG achieves a startup flow velocity as low as 0.211 m·s$^{-1}$ and a peak output voltage of 1.81 V. Across the tested velocity range, the output signal frequency maintains a strong linear correlation with flow velocity ($R^2 = 0.9893$), indicating excellent sensitivity under low-flow conditions. Furthermore, fluid-structure interaction (FSI) simulations conducted in ANSYS Fluent validate the underlying VIV-driven signal generation mechanism and provide theoretical support consistent with experimental observations. This work offers a compelling solution for real-time, energy-autonomous flow sensing in resource-constrained marine environments and holds application prospects in intelligent marine systems.**

## 1. Introduction

Ocean flow field monitoring serves as a fundamental technology for ensuring marine ecological security, facilitating sustainable resource development, and advancing intelligent underwater operations.[1–3] Among the key hydrodynamic parameters, flow velocity serves as a critical indicator.[4] Therefore, it is necessary to investigate the development of highly sensitive, durable, and long-term stable flow velocity sensors, particularly those suited for low-velocity marine environments.

Z. Zhuo, P. Li, S. Li, J. Si, H. Du, A. Liu, Y. Zhang, Y. Zou, M. Xu
State Key Laboratory of Maritime Technology and Safety, Marine Engineering College
Dalian Maritime University
Dalian 116026, China
E-mail: sjc@dlmu.edu.cn; zouyj0421@dlmu.edu.cn; xuminyi@dlmu.edu.cn

The ORCID identification number(s) for the author(s) of this article can be found under https://doi.org/10.1002/admt.202501681

**DOI: 10.1002/admt.202501681**

Typical ocean currents are characterized by relatively low and stable flow velocities often below 0.5 m·s$^{-1}$,[4] accompanied by complex fluctuations. Such characteristics impose stringent performance requirements on sensing systems, particularly in terms of sensitivity, resolution, and operational stability. At present, the primary sensing mechanisms for ocean current velocity monitoring include mechanical,[5,6] electromagnetic,[7,8] acoustic,[9,10] and optical.[4,11] However, these sensing technologies face inherent limitations in marine environments. Specifically, mechanical sensors are prone to corrosion and require frequent maintenance,[12] electromagnetic sensors suffer from electromagnetic interference and rely on continuous external power,[13] acoustic sensors, though widely used, are costly and sensitive to turbidity.[10] Similarly, optical sensors are affected by complex underwater topography and typically require complicated system integration to ensure measurement accuracy.[14,15]

Triboelectric nanogenerators (TENGs) have emerged as a promising technology for intelligent sensing since their introduction in 2012, owing to their high sensitivity, self-powered operation, simple structure, low cost, and broad material compatibility.[16–23] Their excellent signal-to-noise ratio and responsiveness to weak mechanical stimuli make them particularly well-suited for sensing applications in low-velocity underwater environments. Recent studies have demonstrated the capability of TENGs to directly convert physical stimuli, such as fluid kinetic energy and structural deformation, into electrical signals.[24–31] However, underwater low-speed flows differ significantly from atmospheric flows: they generate weaker excitation, are subject to multi-source disturbances, and have lower energy density, all of which place stringent demands on a lower activation threshold, higher interference resistance, and long-term stability.

To address these challenges, researchers have developed a variety of bio-inspired or structurally optimized TENG architectures—including spherical rotors,[32] turbine blades,[33,34] seal-whisker analogues,[35,36] fish-tail cantilevers,[37] and

 

fluttering flags[38–41]—that enhance responsiveness to subtle hydrodynamic perturbations. For example, Cheng et al.[32] designed a fully enclosed self-powered active spherical triboelectric velocity sensor (SASTS) capable of high-precision, high-stability velocity detection across 0.5–500 rpm (2 to 16 $m \cdot s^{-1}$) with long-term stability (≈6 months). Zhang et al.[33] proposed a hybrid triboelectric-electromagnetic sensor that converts fluid-driven rotor motion into reciprocating movement of an internal spring-magnet assembly, enabling both energy harvesting and velocity sensing in the range of 0.5–3 $m \cdot s^{-1}$. To eliminate reliance on external power, Wang et al.[34] introduced vertical-axis turbine-type hybrid sensor that operates entirely self-powered and exhibits a strong linear relationship between output frequency and flow velocity ($R^2 = 0.98$). These advances underscore the promise of TENG-based architectures for reliable, long-term monitoring of low-velocity ocean currents.

Although the aforementioned devices perform well under medium-to-high flow velocities, they typically exhibit high start-up thresholds and slow dynamic responses at low speeds, limiting their applicability for background ocean currents. In this context, flexible biomimetic TENGs have emerged as a promising alternative due to their mechanical compliance and ability to capture weak hydrodynamic perturbations. Wang et al.[35] developed an underwater biomimetic seal-whisker (UBWS) TENG that detects vortex shedding through passive structural vibration, and achieved a linear coefficient of 0.9946 between output voltage and the dimensionless parameter $D \cdot L^{-1}$ (where D is the distance from a vibrating fish-tail and L is the whisker length). Liu et al.[36] Further developed a triboelectric whisker sensor array (TWSA) combined with deep-learning algorithms for 3D flow perception and unmanned-underwater-vehicle (UUV) motion tracking. The system demonstrated a response time of 19 ms, sensitivity 0.2 V $m \cdot s^{-1}$, and signal-to-noise ratio of 58 dB. Moreover, the deep-learning model identified wake frequencies with at least 81.2% accuracy, and achieved a root-mean-square error (RMSE) of ≈0.02. To mitigate the limited contact area and low output typical of whisker structures, Zhang et al.[37] proposed a soft fish-tail TENG (TE-SFT) driven by vortex-induced vibration (VIV), capable of simultaneous energy harvesting and velocity sensing in flows ranging from 0.24 to 0.89 $m \cdot s^{-1}$. The device achieved a power density of 5.56 $W \cdot m^{-3}$ and maintained stable performance after 30 days of immersion.

Despite the favorable disturbance-response characteristics of flexible biomimetic TENGs, their practical deployment remains constrained by several factors, including limited effective contact area, signal instability caused by complex structural deformations, and incomplete mapping between flow velocity and electrical output. Recently, VIV generated by upstream bluff bodies has attracted attention as a more controllable excitation mechanism. When integrated with flag-shaped TENGs, VIV can significantly enhance sensing performance and energy output, reduce start-up flow velocity, simplify structural design, and improve tolerance to turbulent flow disturbances.[38–41] Optimizing bluff-body geometry has been shown to increase output by up to 170% and reduce the start-up velocity to below 0.5 $m \cdot s^{-1}$. Building on this, Han et al.[38] proposed refined geometric design strategies for bluff bodies to reduce the cut-in wind speed and expand the energy harvesting range, while Huang et al.[39] employed composite film materials to improve the compliance and charge retention of the triboelectric layers, further enhancing energy conversion efficiency and operational stability. These advancements highlight the potential of VIV-coupled, flag-shaped TENGs as a promising solution for self-powered, ultra-low-velocity flow monitoring.

Moreover, the vortex-shedding frequency produced by an upstream bluff body follows the classical Strouhal relation, showing an approximately linear dependence on flow velocity across a wide Reynolds number range.[42] This intrinsic linearity offers a robust theoretical basis for mapping output frequency to ambient flow speed and helps mitigate signal crosstalk in noisy underwater environments. However, while bluff-body-driven flag-shaped TENGs have been studied for energy harvesting, their quantitative sensing applications remain underexplored. Two main research gaps persist: i) the lack of a well-defined transfer function linking electrical output to true flow velocity, and ii) insufficient theoretical and numerical validation of the sensing mechanism.

To address these challenges, the present work proposes an underwater cylinder-enhanced flag-shaped triboelectric nanogenerator (UCF-TENG) that integrates VIV excitation with a flag-shaped TENG, aiming to overcome both the high start-up threshold and the lack of a clear sensing model in conventional devices. The research integrates theoretical analysis, experiments, and numerical simulation to validate its strong physical interpretability. First, charge-transfer and vibration-response models are developed to examine how key structural parameters-such as the bluff-body diameter and its spacing from the triboelectric flag-affect output performance and sensing sensitivity, thereby identifying an optimal configuration. Second, fluid-structure interaction (FSI) simulations in ANSYS Fluent are performed to compare VIV excitation efficiency across different bluff-body geometries, verify the experimentally observed velocity–frequency relationship, and construct a complete hydrodynamic sensing model. Finally, a wireless prototype system incorporating a signal acquisition and transmission module is implemented and tested, in order to demonstrate the UCF-TENG's real-time flow sensing capability and integration potential under representative underwater conditions.

## 2. Model and Mechanism

### 2.1. Design and Working Mechanism of UCF-TENG

To address the challenges of ultra-low-velocity flow sensing in marine environments, this work proposes an underwater cylinder-enhanced flag-shaped triboelectric nanogenerator (UCF-TENG) by vortex-induced vibration (VIV). When periodic vortices are shed from an upstream bluff body, a Kármán vortex street forms in the wake, inducing lateral oscillations of the sensing unit. These oscillations generate cyclic contact and separation between internal triboelectric layers, converting mechanical energy into electrical output. The conceptual schematic is shown in **Figure 1a**. The UCF-TENG consists of two components: i) a sensing unit, and ii) an upstream-mounted cylindrical bluff body. As depicted in Figure 1b-i, the fundamental sensing unit comprises a central polytetrafluoroethylene (PTFE) film and two graphite-printed polyethylene terephthalate (PET) electrode layers, as shown in Figure S1a (Supporting Information). These flexible, conductive layers are chosen for their suitability in underwater triboelectric applications. To enhance surface charge

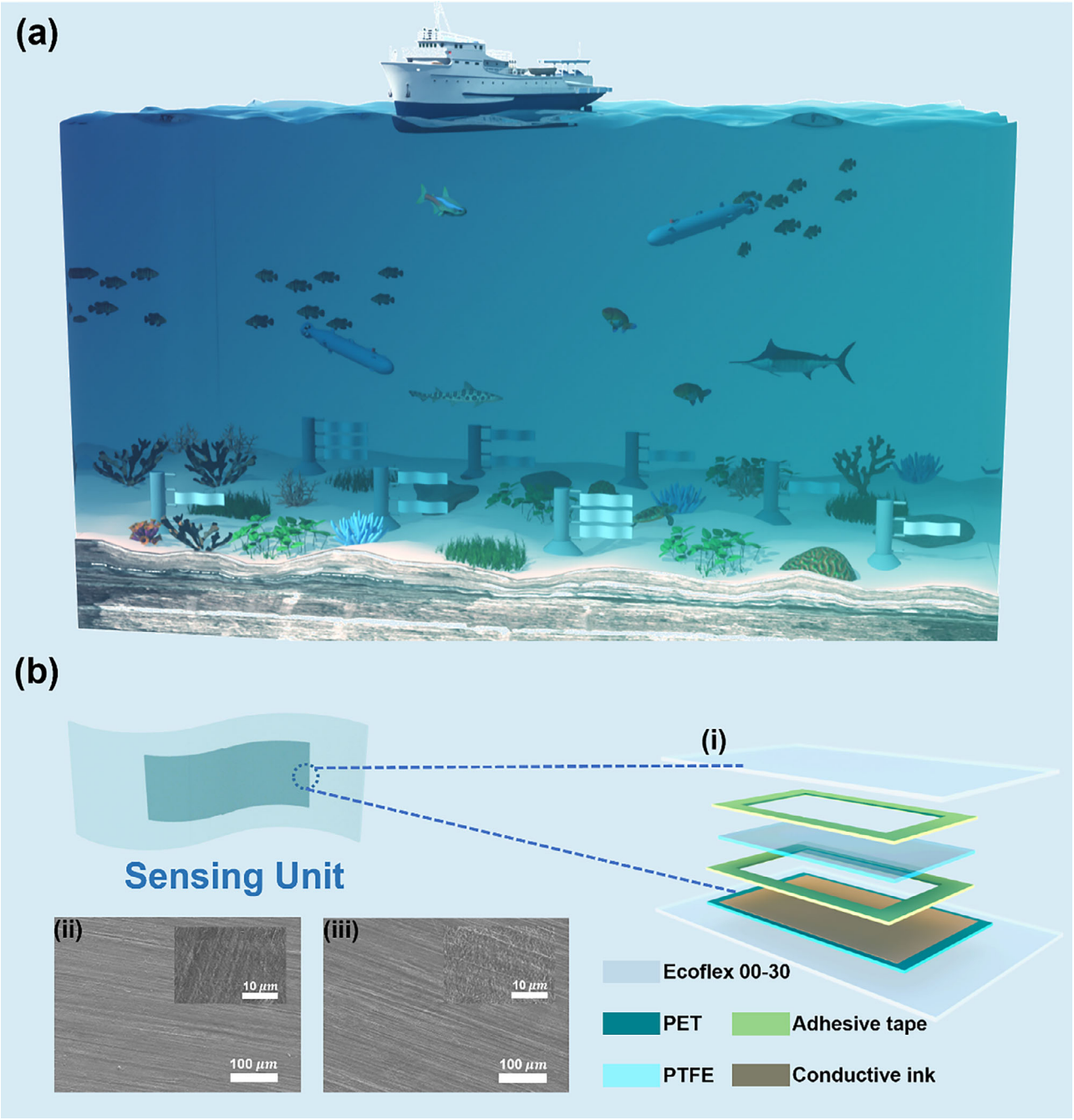


**Figure 1.** Application scenario and structure of UCF-TENG. a) Application scenario of the UCF-TENG. b) Schematic diagram of the Sensing Unit of the UCF-TENG.

density and contact efficiency, the films are mechanically polished with 10000-grit sandpaper. The resulting microstructures are shown in Figure 1b-ii,iii. The entire assembly is encapsulated in Ecoflex 00–20 silicone, ensuring waterproofing, mechanical flexibility, and long-term stability in submerged conditions, as shown in Figure S1b (Supporting Information). Distinct from the optimization of similar thin-film TENGs for high-power energy harvesting, as in the notable work by Tao et al.,[43] the monolithic silicone encapsulation strategy proposed herein is tailored for sensing applications, as it ensures not only the device's underwater robustness but also the highly predictable mechanical response required for signal fidelity, thereby broadening the application scope of such TENGs into in-situ environmental monitoring.

The bluff body plays a critical role in generating periodic hydrodynamic excitation. As fluid flows past the bluff body, alternating vortex shedding produces dynamic wake forces that drive the flag to oscillate. To determine the

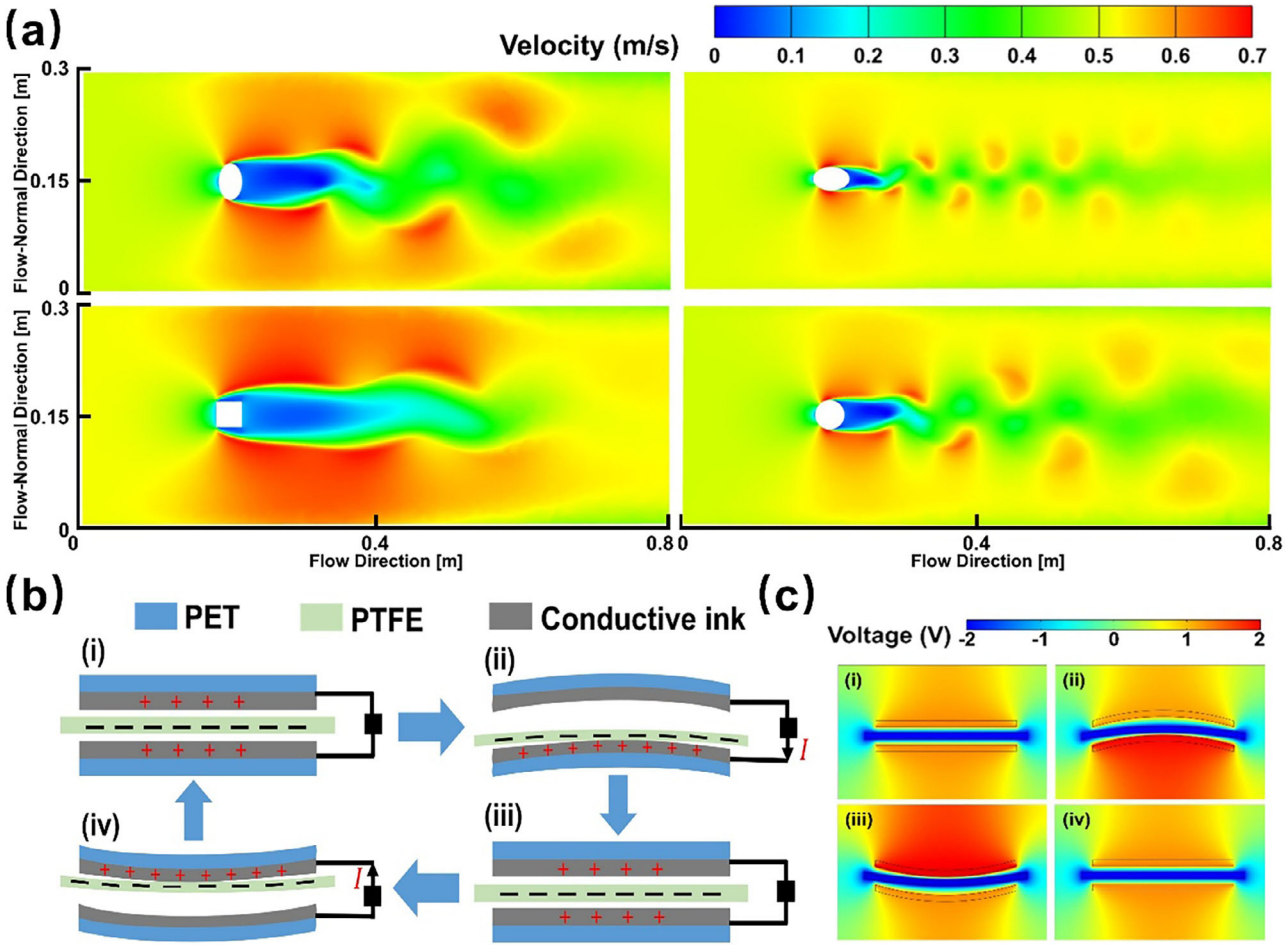


**Figure 2.** Numerical simulation of front-mounted bluff body configuration and operational principle in UCF-TENG power generation. a) Numerical simulations of flow around cylindrical bluff bodies with elliptical, square, and circular cross-sections conducted under identical conditions. b) Working mechanism of the Sensing Unit the UCF-TENG. c) COMSOL simulation of the periodic potential change between the two electrodes of the Sensing Unit the UCF-TENG.

optimal geometry, fluid-structure interaction (FSI) simulations were conducted using ANSYS Fluent, evaluating three typical cross-sectional shapes: circular, elliptical (two placement methods), and rectangular. As shown in **Figure 2**a, the circular section demonstrated the most stable vortex street and highest excitation efficiency and was selected for final implementation.

The operating cycle for the sensing unit the UCF-TENG is illustrated in Figure 2b. Initially, as shown Figure 2b-i, the PTFE film is suspended between the two electrodes without contact, maintaining electrostatic balance via triboelectric induction. When the sensing unit oscillates laterally, the PTFE film first contacts the lower electrode, as shown in Figure 2b-ii, generating a potential difference that drives electron flow through the external circuit. As the sensing unit responds to periodic vortex shedding and oscillates in the opposite direction, the PTFE film subsequently contacts the upper electrode as shown in Figure 2b-iv, completing one full alternating current (AC) cycle. This contact–separation mechanism was further validated using electrostatic field simulations performed in COMSOL Multiphysics (Figure 2c).

Based on the contact-mode independent-layer TENG theory, the output voltage, the output voltage $V$ can be expressed as follows:[44]

$$V_{oc} = -\frac{1}{C} + V_{oc} = -\frac{d_0 + g}{\epsilon_0 S} Q + \frac{2\sigma x}{\epsilon_0} \quad (1)$$

where $C$ is the total output charge, $V_{oc}$ is the open-circuit voltage, and $C$ is the capacitance of the TENG. Specifically, $d_0$ denotes the thickness of the PTFE layer, $g$ is the distance between two electrodes, $\epsilon_0$ is the permittivity of free space, $S$ is the electrode area, $x$ is the displacement between the PTFE membrane and electrode, and $\sigma$ is the charge density.

### 2.2. Theoretical Model of UCF-TENG

#### *2.2.1. Kinematic Characteristics of VIV*

According to Kármán vortex street theory, when fluid flows past a bluff body, periodic vortex shedding occurs, generating an unsteady pressure field in the wake region.[42] Placing a flexible

structure in this wake leads to amplified oscillations due to flow-structure resonance, significantly enhancing the energy harvesting efficiency of the UCF-TENG, especially in ultra-low-velocity flow conditions. In the UCF-TENG, the oscillation of the flag is not a simple flutter phenomenon but results from the combined action of steady fluid forces and vortex-shedding-induced excitations, forming a composite flow-induced vibration. Furthermore, the use of flexible silicone encapsulation, introduced in this work for the first time, intentionally increases the overall structural stiffness and damping. This design choice serves to suppress unpredictable, high-order flutter and promotes a dominant, first-order oscillation, thereby aligning the sensor's physical behavior more closely with the assumptions of the elastic beam vibration model used for analysis.

To capture these dynamics, a fluid-structure interaction (FSI) model of the UCF-TENG is developed using ANSYS Fluent, as shown in **Figure** 3a,b. As illustrated in Figure 3c-i,ii, high-velocity flow regions beneath the cylinder and low-velocity regions above it generates downward-directed lift forces during this phase, inducing downward vibration of the sensing unit. Conversely, when the high- and low-velocity regions exchange positions in the subsequent phase (Figure 3c-iii,iv), upward lift forces emerge, driving upward vibration. Movie S1 (Supporting Information) demonstrates the concrete vibration dynamics of the system. Simultaneously, simulation results (Figure 3c) indicate that the system predominantly operates in its first-order vibration mode under stable marine flow conditions, allowing for a simplified linear modal analysis in subsequent modeling.

Drawing inspiration from the vibration model developed by Allen and Smits,[45] the UCF-TENG's oscillation is described as the superposition of wake-induced vibration ($f_1$) and self-excited vibration ($f_2$). Therefore, the governing equation for this composite flow-induced vibration can be expressed as:

$$m\ddot{y}(t,x) + H(\ddot{y}, y, x, t) = f_1 + f_2 \tag{2}$$

where $y(t, x)$ is the structural displacement in the wave direction, $m$ is the structural mass, and $H$ is the internal restoring force related to the object stiffness and damping characteristics. $f_1$ represents excitation due to vortex shedding, and $f_2$ represents force induced by steady water flow. This composite vibration model provides a theoretical basis for analyzing the dynamic coupling between hydrodynamic excitation and the mechanical-electrical response of the UCF-TENG. It also supports the subsequent development of velocity-frequency mapping strategies essential for sensing calibration.

#### 2.2.2. Vortex Shedding Mechanism

When uniform flow encounters a bluff body and the velocity exceeds a critical threshold, periodic vortex shedding occurs in the wake region. This phenomenon induces oscillatory forces on downstream structures, leading to regular mechanical vibrations.[42] The vortex shedding frequency $f$ follows the classical Strouhal relation:[46]

$$f = S_t \times \frac{U}{L} \tag{3}$$

where $S_t$ is the Strouhal number, $U$ is the free-stream flow velocity, and $L$ is the characteristic length of the bluff body. The Strouhal number $S_t$ is primarily a function of the Reynolds number $Re$ which $Re$ is defined as:

$$Re = \frac{\rho U L}{\nu} \tag{4}$$

where $\rho$ is the fluid density, $U$ is the free-stream flow velocity, $L$ is the characteristic length of the bluff body; $\nu$ is the dynamic viscosity of water. In the subcritical flow regime ($Re < 3 \times 10^5$), the $S_t$ number remains nearly constant, ranging from 0.18 to 0.21.[47] This approximately linear relationship between vortex shedding frequency and ambient flow velocity is critically important for establishing an interpretable and physically grounded sensing mechanism in flow velocity measurement systems.

## 3. Results and Discussion

### 3.1. Electrical Output Performance of the UCF-TENG

**Figure** 4a illustrates the experimental setup of the UCF-TENG in a circulating flume. A honeycomb flow straightener is used to maintain uniform and low-turbulence inflow. The UCF-TENG device is fixed on a rigid support, and its open-circuit voltage and short-circuit current are measured using an electrometer over a flow velocity range of 0.211–0.499 m·s$^{-1}$. The detailed descriptions of these devices will be presented in the Experimental Section.

Figure 4b illustrates key understudied parameters influencing the electrical output performance of the UCF-TENG. Figure 4c,d shows the output voltage and current of the UCF-TENG under different flow velocities. Both signals increase with velocity, reflecting stronger vortex-induced excitations at higher speeds. The electrical output is also affected by the cylinder diameter, which modulates the strength and structure of the wake, thereby influencing the oscillation amplitude of the sensing unit. Since the sensing unit 's structural parameters remain constant, optimizing the cylinder size and spacing is critical for tuning its dynamic response.

Figure 4e–j presents the influence of cylinder diameter and spacing on electrical performance. The results show a non-monotonic relationship: neither voltage nor current increases uniformly with size. At the maximum tested velocity (0.499 m·s$^{-1}$), the 50 mm bluff body achieves the highest output, generating 1.39 V and 18.41nA. The 75 mm configuration produces moderate output (0.86 V, 13.97 nA), while the 25 mm diameter yields the lowest (0.78 V, 11.02 nA), as further demonstrated in Figure S2 (Supporting Information). This nonlinear behavior arises from the interaction between vortex shedding frequency and pressure gradient effects. Larger bluff bodies reduce shedding frequency due to increased flow separation, but amplify downstream pressure differences. Although higher pressure gradients can enhance oscillation amplitude, they also increase compressive forces on the triboelectric layers, reducing the effective contact-separation cycles and limiting charge generation. Conversely, too small a bluff body produces insufficient wake excitation to effectively drive the TENG. These findings highlight the need to select an optimal bluff body diameter that balances wake

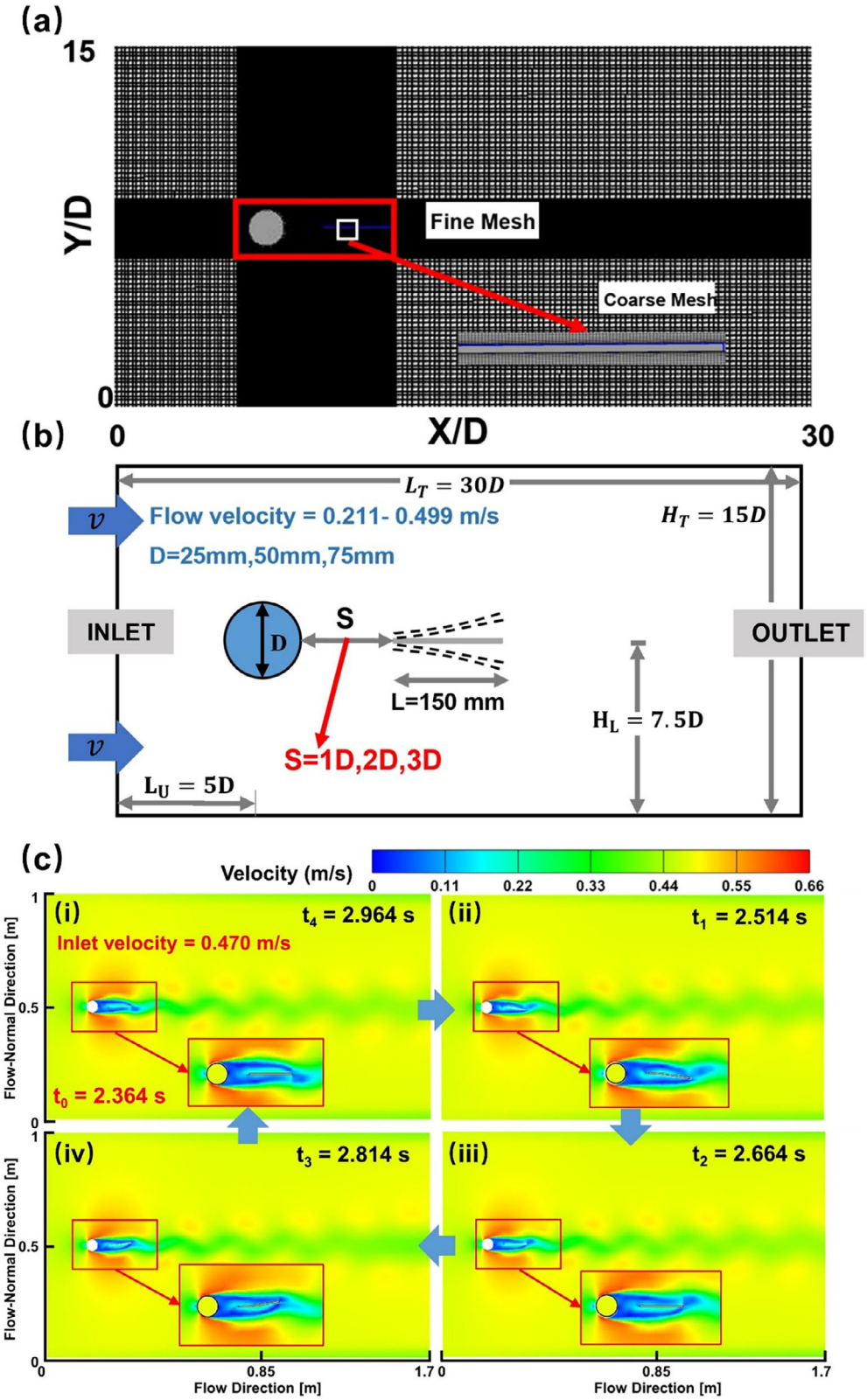


**Figure 3.** Schematic diagram of ANSYS simulation. a,b) The fluid-structure interaction (FSI) model of the UCF-TENG is developed using ANSYS Fluent. c) Numerical simulation of underwater kinematic states for UCF-TENG in ANSYS Fluent.

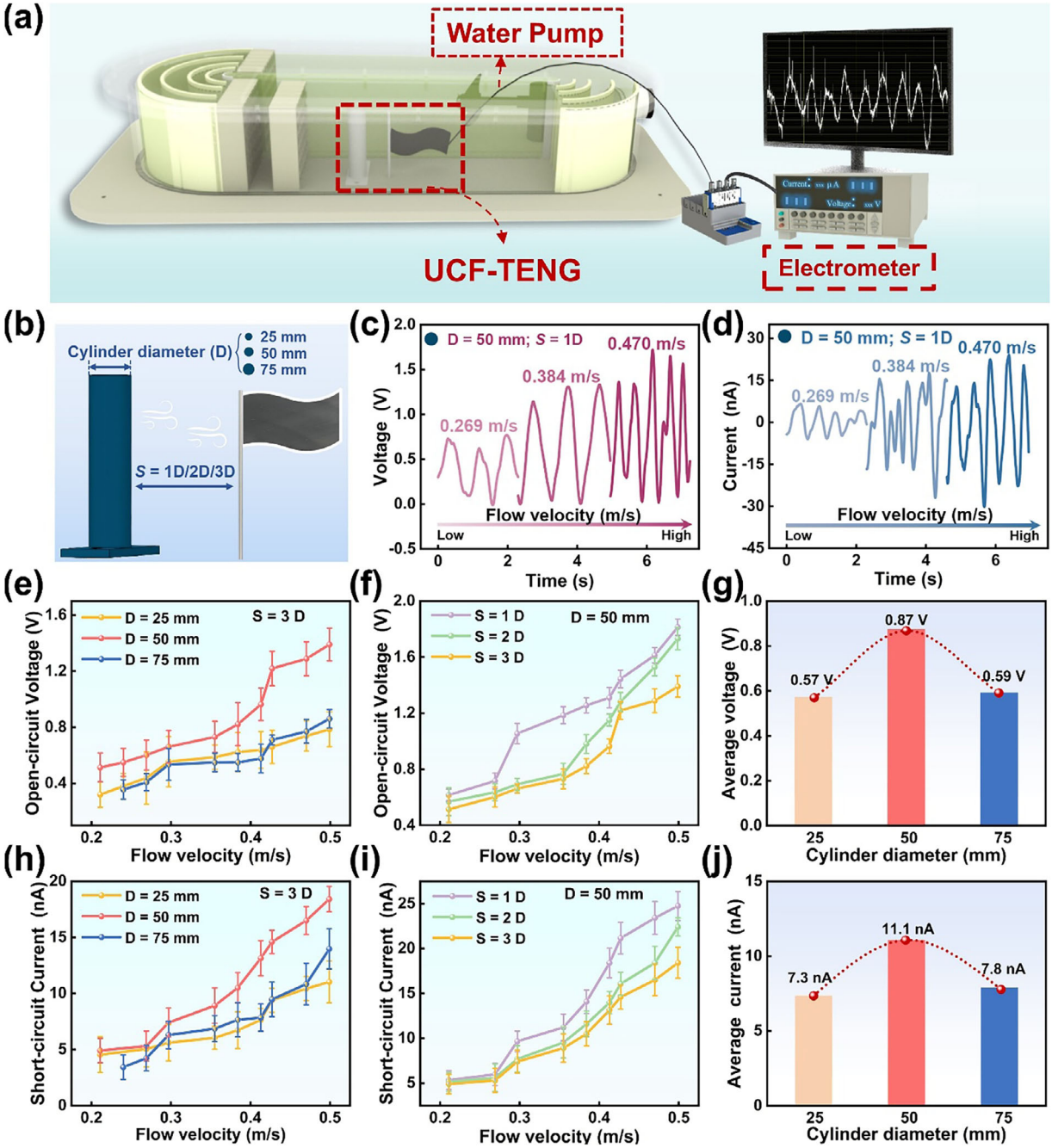


**Figure 4.** Output characteristics of the UCF-TENG under different flow velocity. a) Underwater experimental platform. b) Parameters that need to be explored for the device. c,d) The initial voltage and current signals of the proposed sensor under specific conditions. e) The output voltages of sensors for different cylinder diameters and S = 3D. f) The output voltages of sensors from S = 1-3D and D = 50 mm. g) The overall average voltage. h) The output current of sensors for different cylinder diameters and S = 3D. i) The output current of sensors from S = 1-3D and D = 50 mm. j) The overall average current.

excitation with mechanical compliance to maximize energy conversion under low-speed flow conditions.

To ensure statistical reliability, outputs were averaged across all spacing conditions. The 50 mm cylinder diameter consistently exhibited superior performance in both voltage and current compared to the other diameters tested. Figure 4f,i further analyze the effect of streamwise spacing between the cylinder and the sensing unit under the 50 mm diameter configuration. Both voltage and current outputs decrease as spacing increases, mainly due to the gradual decay of the Kármán vortex street downstream. Reduced vortex strength weakens flag oscillation, leading to fewer contact–separation cycles and diminished triboelectric output.

In addition to signal amplitude, the frequency characteristics of the UCF-TENG output are crucial for flow velocity

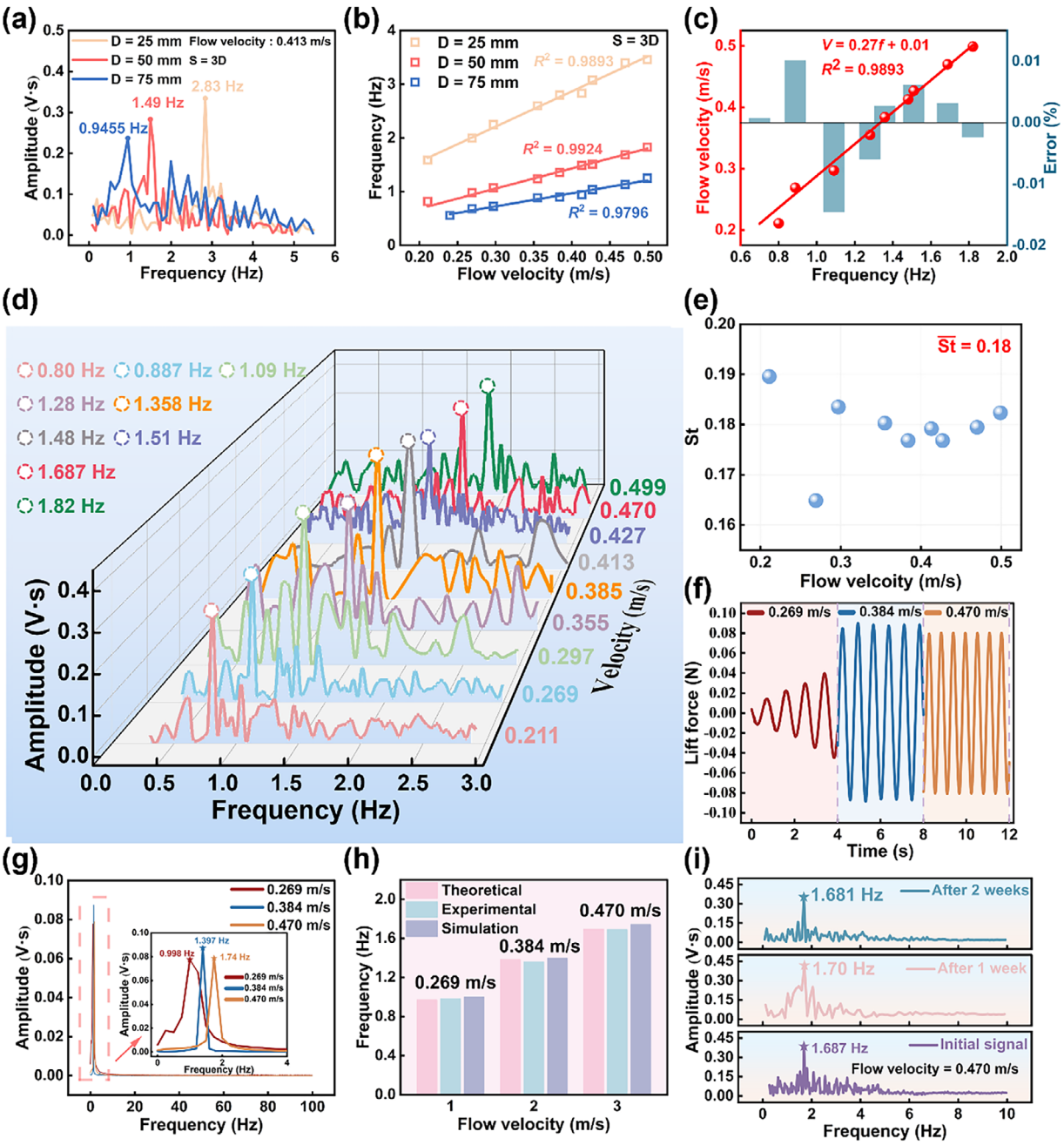


**Figure 5.** The flow velocity sensing performance and simulation results of the optimized sensor structure (with D = 50 mm and S = 1D). a) The amplitude plots at different cylinder diameters, $v = 0.413\ m{\cdot}s^{-1}$, S = 3D. b) Flow velocity-frequency relationship of different cylinder diameters and S = 3D. c) Flow velocity-frequency relationship from 0.211 to 0.499 $m{\cdot}s^{-1}$. d) The amplitude plots at different flow velocities. e) The Strouhal number distribution range and mean from 0.211 to 0.499 $m{\cdot}s^{-1}$. f) The lift curve at different flow velocities. g) Frequency domain representation of lift curve derived from FFT. h) Comparison of the theoretical, experimental, and simulation frequency at flow velocities for the UCF-TENG. i) Durability test result of the UCF-TENG within two weeks.

sensing, as they directly determine velocity resolution. **Figure** 5a shows the FFT spectra of the output signals under different cylinder diameters and S = 3D, as further demonstrated in Figures S3–S5 (Supporting Information). Figure 5b shows the flow velocity-frequency relationship of different the cylinder diameter and S = 3D. Across the full velocity range, a strong linear correlation is observed between flow velocity and signal frequency, with correlation coefficients ($R^2$) consistently exceeding 0.95. Among all tested configurations, the 50 mm cylinder not only delivers the highest signal amplitude but also provides the most distinct spectral peaks and the best frequency–velocity resolution, reaffirming its optimal performance for both energy harvesting and ultra-low-velocity flow sensing.

### 3.2. Flow Velocity Sensing Performance of UCF-TENG

Based on the optimized configuration identified in Section 3.1, a 50 mm-diameter cylindrical bluff body placed at a streamwise distance of 1D from the flag—the flow velocity sensing performance of the UCF-TENG was systematically evaluated. Figure 5c presents the relationship between the dominant output frequency of the UCF-TENG voltage signal and the flow velocity over the range of 0.211–0.499 m·s$^{-1}$. The results fit the linear model $v = 0.27f + 0.01$ with a correlation coefficient of $R^2 = 0.9893$, confirming a stable and precise linear correlation between output frequency and flow velocity. The FFT spectra in Figure 5d display clear single-frequency peaks at each velocity, demonstrating high signal integrity and minimal spectral noise under submerged conditions. Further validation is provided by calculating the Strouhal number from the measured frequencies (Figure 5e). The results are tightly clustered around $S_t \approx 0.18$, in good agreement with the classical sub-critical regime of $S_t \in (0.18, 0.21)$ for $Re < 3 \times 10^5$.[47] This agreement reinforces the physical validity of the UCF-TENG's frequency-based sensing mode.

To exclude experimental artefacts and verify the sensing mechanism, a FSI simulation was performed in ANSYS Fluent (Figure 3a,b). The simulation employed no-slip boundary conditions on the bluff body, symmetry planes at the lateral walls, and a uniform inlet velocity matching experimental conditions (0.269, 0.384, and 0.470 m·s$^{-1}$). The SST $k$–$\omega$ model was used to capture near-wall flow effects. The simulated time-resolved lift force on the bluff body (Figure 5f) exhibited a clear periodic signature corresponding to vortex shedding. The FFT analysis of this lift force (Figure 5g) identified a dominant frequency that matches the primary spectral component of the electrical output. Comparative results from simulation, Strouhal theory, and experimental measurements (Figure 5h) show excellent consistency, confirming the robustness of the sensing mechanism across theoretical, numerical, and experimental domains.

In addition to accuracy, the long-term operational stability of the UCF-TENG was evaluated through one-week and two-weeks immersion tests. As shown in Figure 5i, the dominant output frequency remained stable throughout the testing period, demonstrating excellent durability and reliability in underwater environments. Collectively, these results establish the UCF-TENG as a reliable, linear, and stable platform for continuous monitoring of ultra-low-velocity marine currents, with strong potential for integration into autonomous oceanographic instrumentation and long-term marine observation networks.

### 3.3. UCF-TENG for Practical Flow Velocity Monitoring Applications

To verify the system-level applicability of the UCF-TENG in real-time underwater flow sensing, a wireless flow velocity monitoring system was developed and tested. The system architecture is shown in Figure S6 (Supporting Information). The UCF-TENG, operating based on VIV, generates periodic voltage signals corresponding to ambient hydrodynamic excitations. These signals are processed in real time using the frequency–velocity calibration model established in Section 3.2.

The voltage output is first acquired by an Arduino Nano microcontroller, which performs digital filtering to suppress underwater noise. An onboard FFT then extracts the dominant frequency of signal. Using the pre-determined calibration equation $v = 0.27f + 0.01$, the system calculates the corresponding flow velocity. The processed data is wirelessly transmitted via a LoRa 1276X module to a remote receiver, where real-time velocity readings are displayed on a host computer. The hardware integration of signal acquisition, processing, and transmission components is detailed in **Figure 6**a,b.

To evaluate system performance, the UCF-TENG wireless monitoring module was tested in a circulating water flume and benchmarked against a commercial flow meter. Upon flow initiation, the UCF-TENG produced stable oscillations, and the system successfully captured, processed, and transmitted the corresponding signals via the Arduino—LoRa communication pipeline. At a test condition where the UCF-TENG reported a velocity of 0.40 m·s$^{-1}$, the commercial flow meter recorded 0.413 m·s$^{-1}$, corresponding to a relative error of 3.15%. This result confirms the accuracy, feasibility, and stability of the UCF-TENG-based wireless sensing system for real-time, self-powered underwater flow monitoring (Figure 6c,d; see also Videos S2 and S3, Supporting Information).

This proof-of-concept demonstration highlights the potential of UCF-TENG technology for deployment in distributed, autonomous marine sensing networks. Its self-powered operation and robust frequency-resolved sensing capability make it particularly suitable for long-term monitoring in low-energy, ultra-low-velocity marine environments, where traditional flow sensors often face limitations related to sensitivity, power consumption, and deployment complexity.

## 4. Conclusion

In conclusion, this study successfully develops and validates an underwater cylinder-enhanced flag-shaped triboelectric nanogenerator (UCF-TENG), establishing a robust framework for quantitative, self-powered sensing in ultra-low-velocity marine environments. Through systematic optimization, the device achieves an exceptionally low startup velocity of 0.211 m·s$^{-1}$. Critically, the novelty of this work is distinguished by three core contributions: i) the establishment of a direct and highly linear ($R^2 = 0.9893$) mapping between flow velocity and output signal frequency, providing a clear, physically-grounded sensing model; ii) a pioneering triangulation methodology that integrates numerical simulations, experimental validation, and theoretical modeling to rigorously confirm the VIV-driven mechanism; and iii) the successful demonstration of a complete wireless monitoring system, validating its practical potential for long-term, autonomous ocean current monitoring. By isolating the core sensing unit with a waterproof flexible silicone encapsulation, the UCF-TENG also ensures environmental robustness for marine applications. Collectively, this work presents a compelling and viable strategy for persistent, real-time monitoring of low-velocity ocean current fields.

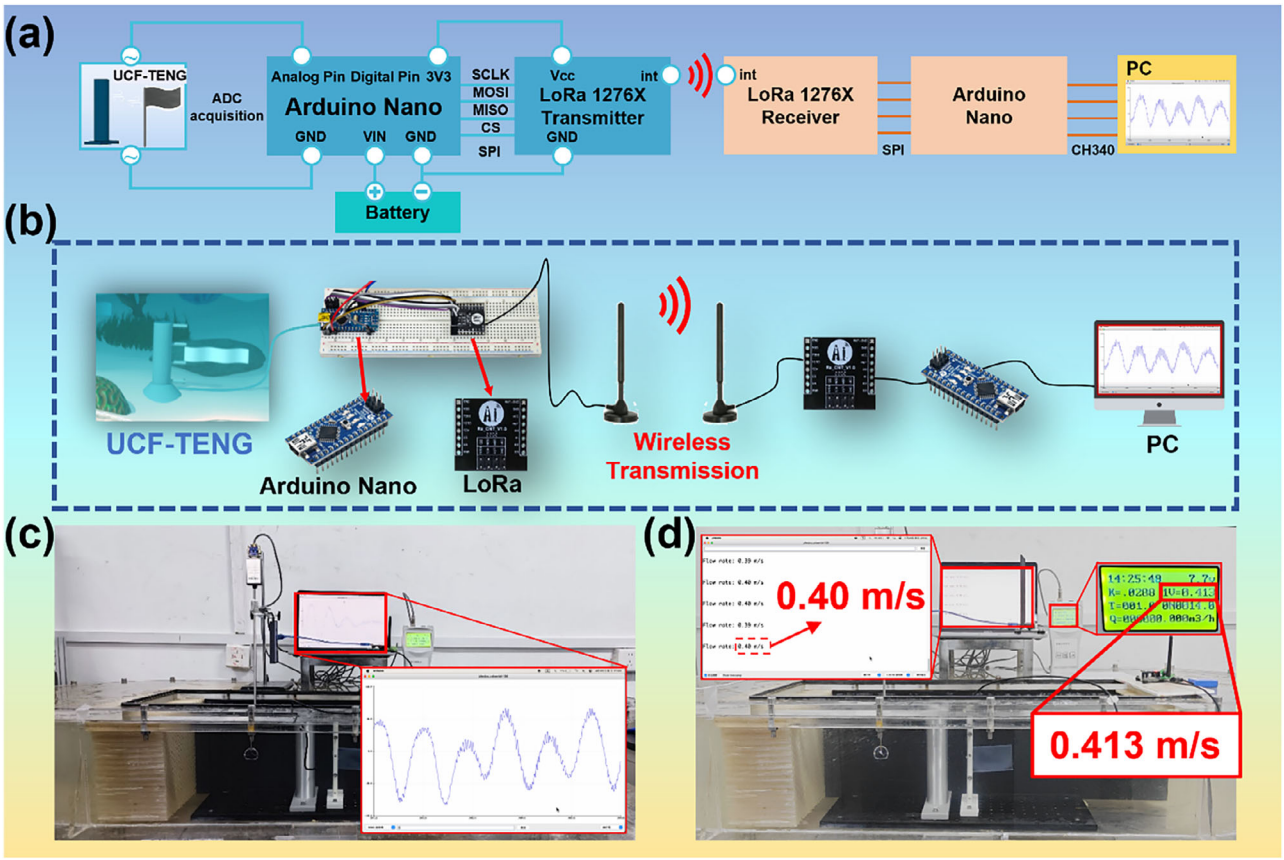


**Figure 6.** The practical application performance of the UCF-TENG. a,b) Workflow of the underwater flow monitoring system. c) Output signal collected by the Arduino Nano. d) Flow velocity output by the Arduino Nano and comparison of UCF-TENG and commercial velocity meter.

## 5. Experimental Section

*Fabrication of UCF-TENG*: The flow velocity sensor (UCF-TENG) proposed herein features a simple structure primarily comprising a cylindrical bluff body and a sensing unit. The cylindrical bluff body was constructed in two parts: a cylindrical main body and a base. Both components were designed and modeled using SolidWorks software and fabricated using 3D printing technology with polylactic acid (PLA) material. For the fabrication of the sensing unit, the procedure is illustrated in Figure 1b-i. The thicknesses of the polytetrafluoroethylene (PTFE) film, polyethylene terephthalate (PET) film, and adhesive tape employed were 30, 25, and 30 µm, respectively. First, conductive ink was screen-printed onto the PET film and dried at room temperature for 24 h to form a flexible electrode. Subsequently, both sides of the PTFE film were carefully abraded using 10000-grit sandpaper to create the triboelectric layer (as shown in Figure 1b-ii,iii)). Thereafter, two flexible electrodes and one PTFE film were assembled into the fundamental power generation unit by bonding with adhesive tape, as depicted in Figure S1a (Supporting Information). Finally, since this power generation unit operates in an underwater environment, it was subjected to waterproof encapsulation using an Ecoflex 00–20 silicone gel to ensure environmental protection, illustrated in Figure S1b (Supporting Information).

*Circulating Flume*: The experimental characterization of the UCF-TENG was conducted in a circulating flume with a test section measuring 0.25 m (width) × 0.25 m (height) × 0.90 m (length). Water flow velocities encompassed a range of 0.133–0.499 $m \cdot s^{-1}$ and were generated using a propeller-driven system, wherein rotational speed was precisely regulated by an inverter-based controller. To ensure measurement accuracy, a calibrated flow meter (LS300-A model) was installed within the test section for real-time velocity verification during all experimental measurements.

*Electrical Measurement*: Electrical output characterization of the UCF-TENG was performed using a dedicated electrometer (Model 6514, Keithley Instruments) to measure open-circuit voltage short-circuit current, and transferred charge. These parameters were simultaneously recorded and visualized via a PC-end LabVIEW program interfacing with the instrument. In the demonstration, an Arduino Nano microcontroller was employed to acquire signals from the UCF-TENG and compute flow velocities in real-time. Through a 433 MHz LoRa Ra-02 wireless module, the processed data was transmitted remotely. The receiving terminal, comprising a paired Arduino Nano and LoRa transceiver, acquired the transmitted results and displayed them on a computer screen.

## Supporting Information

Supporting Information is available from the Wiley Online Library or from the author.

## Acknowledgements

The work was supported by the Scientific Research Innovation Capability Support Project for Young Faculty (Grant No. ZYGXQNJSKYCXNLZCXM-O1P), Fundamental Research Funds for the Central Universities (Grant No. 3132025230), and Fundamental Research Funds from the Department of Education of Liaoning Province (Grant No. LJ212410151008).

## Conflict of Interest

The authors declare no conflict of interest.

## Data Availability Statement

The data that support the findings of this study are available from the corresponding author upon reasonable request.

## Keywords

flow velocity sensor, ocean flow field monitoring, triboelectric nanogenerators, vortex-induced vibration

Received: August 8, 2025
Revised: September 24, 2025
Published online: October 7, 2025

[1] C. P. Buzzelli, *Estuaries* **1998**, *21*, 659.
[2] Q. Xia, N. Song, C. Liu, R. Zhai, C. Ai, X. Sun, S. Zhang, *Sens. Actuators A* **2023**, *351*, 114158.
[3] R. Klaus, D. A. Jones, J. Turner, N. Simöes, D. Vousden, *J. Arid Environ.* **2003**, *54*, 71.
[4] Y. Li, J. Meng, X. Chen, S. Wang, H. Miao, Q. Li, L. Sun, Z. Liu, J. Wang, *Opt. Laser Technol.* **2024**, *175*, 110884.
[5] M. L. Ali, R. Ridoy, U. Barua, M. B. Alamgir, *J. Mater. Sci. Technol* **2016**, *4*, 16.
[6] B. Boman, S. Shukla, *Edis* **2006**, *2006*, 17.
[7] S. Chen, Y. Wu, S. Liu, Y. Yang, X. Wan, X. Yang, K. Zhang, B. Wang, X. Yan, *J. Mar. Sci. Eng.* **2023**, *11*, 206.
[8] Z. Wang, S. Wang, X. Luo, *IEEE Trans. Instrum. Meas.* **2023**, *72*, 1.
[9] S. Catsamas, B. Shi, B. Deletic, M. Wang, D. T. McCarthy, *Sensors* **2022**, *22*, 7451.
[10] S. D. Banjavcic, A. R. Schmidt, *J. Hydraul. Eng.* **2018**, *144*.
[11] Q. Zhao, H.-k. Zheng, R.-q. Lv, Y.-f. Gu, Y. Zhao, Y. Yang, *Sens. Actuators A* **2018**, *280*, 68.
[12] P. Hosegood, H. van Haren, *Deep Sea Res. Part I* **2003**, *50*, 657.
[13] K. Chen, Q. Zhao, M. Deng, X. Luo, J. Jing, *Earth, Planets Space* **2020**, *72*, 4.
[14] L. Wangxu, L. Zhenggui, D. Wanquan, J. Lei, Q. Yilong, C. Huiyu, *Flow Meas. Instrum.* **2021**, *82*, 102072.
[15] H. Chen, Y. Qiu, H. Wang, M. Gao, *Processes* **2024**, *12*, 144.
[16] C. Pan, L. N. Y. Cao, J. Meng, L. Jia, W. Hu, Z. L. Wang, X. Pu, *Energy Environ. Sci.* **2024**, *17*, 1132.
[17] M. Guo, Y. Xia, J. Liu, Y. Zhang, M. Li, X. Wang, *Adv. Funct. Mater.* **2025**, *35*, 2419209.
[18] S. Hu, Z. Ge, M. Chen, P. Ding, W. Zhai, G. Zheng, K. Dai, C. Liu, C. Shen, *Chem. Eng. J.* **2025**, *510*, 161794.
[19] S. Jia, X. Yang, W. Feng, L. Liu, L. Zhao, L. Wu, S. Li, W. Zuo, Q. Tang, T. Jiang, Z. Wang, *Small* **2025**, *21*, 2501073.
[20] X. Li, P. Wang, C. Zong, H. Niu, P. Xu, Y. Yu, Y. Li, G. Shen, *Nano Energy* **2025**, *140*, 110995.
[21] Y. Zhang, X. Cao, Z. L. Wang, *Nano Energy* **2023**, *108*, 108210.
[22] Z. Wang, J. Wang, Z. Yang, J. Zhu, P. Zhang, X. Yu, H. Li, Y. Yu, Y. Zhang, Z. L. Wang, T. Cheng, *Energy Environ. Sci.* **2025**, *18*, 3761.
[23] C. Zhang, Y. Hao, X. Lu, W. Su, H. Zhang, Z. L. Wang, X. Li, *Nano-Micro Lett.* **2025**, *17*, 124.
[24] Y. Xi, H. Guo, Y. Zi, X. Li, J. Wang, J. Deng, S. Li, C. Hu, X. Cao, Z. L. Wang, *Adv. Energy Mater.* **2017**, *7*, 1602397.
[25] X. Fu, S. Xu, Y. Gao, X. Zhang, G. Liu, H. Zhou, Y. Lv, C. Zhang, Z. L. Wang, *ACS Energy Lett.* **2021**, *6*, 2343.
[26] C. Ge, J. Ma, Y. Hu, J. Li, Y. Zhang, X. He, T. Cheng, J. Wen, *Adv. Mater. Technol.* **2022**, *8*, 2201269.
[27] M. Xu, Y.-C. Wang, S. L. Zhang, W. Ding, J. Cheng, X. He, P. Zhang, Z. Wang, X. Pan, Z. L. Wang, *Extreme Mech. Lett.* **2017**, *15*, 122.
[28] W. Li, L. Lu, X. Fu, C. Zhang, K. Loos, Y. Pei, *ACS Appl. Mater. Interfaces* **2022**, *14*, 51018.
[29] M. Olsen, R. Zhang, J. Örtegren, H. Andersson, Y. Yang, H. Olin, *Sci. Rep.* **2019**, *9*, 5543.
[30] G. Shen, J. Ma, Y. Hu, J. Li, T. Cheng, J. Wen, *Sensors* **2022**, *22*, 4832.
[31] Y. Wang, E. Yang, T. Chen, J. Wang, Z. Hu, J. Mi, X. Pan, M. Xu, *Nano Energy* **2020**, *78*, 105279.
[32] P. Cheng, M. Sun, C. Zhang, H. Guo, J. Shi, Y. Zhang, Y. Liu, J. Wang, Z. Wen, X. Sun, *IEEE Trans. Nanotechnol.* **2020**, *19*, 230.
[33] Q. Zhang, L. Li, T. Wang, Y. Jiang, Y. Tian, T. Jin, T. Yue, C. Lee, *Nano Energy* **2021**, *90*, 106501.
[34] Y. Wang, Z. Qian, C. Zhao, Y. Wang, K. Jiang, J. Wang, Z. Meng, F. Li, C. Zhu, P. Chen, H. Wang, M. Xu, *Adv. Mater. Technol.* **2022**, *8*, 2201245.
[35] S. Wang, P. Xu, X. Wang, J. Zheng, X. Liu, J. Liu, T. Chen, H. Wang, G. Xie, J. Tao, M. Xu, *Nano Energy* **2022**, *97*, 107210.
[36] B. Liu, B. Dong, H. Jin, P. Zhu, Z. Mu, Y. Li, J. Liu, Z. Meng, X. Zhou, P. Xu, M. Xu, *Adv. Mater. Technol.* **2024**, *10*, 2401053.
[37] S. Zhang, Z. Jing, X. Wang, M. Zhu, X. Yu, J. Zhu, T. Cheng, H. Zhao, Z. L. Wang, *Nano Res.* **2022**, *16*, 466.
[38] Y. Han, F. Wu, X. Du, Z. Li, H. Chen, D. Guo, J. Wang, H. Yu, *Nano Energy* **2024**, *119*, 109063.
[39] X. Huang, C. Xing, Z. Zhou, S. Zuo-Jiang, D. Sun, G. Chen, X. Jiang, *Nano Energy* **2025**, *135*, 110664.
[40] Y. Wang, X. Liu, T. Chen, H. Wang, C. Zhu, H. Yu, L. Song, X. Pan, J. Mi, C. Lee, M. Xu, *Nano Energy* **2021**, *90*, 106503.
[41] W. Sun, Z. Ding, Z. Qin, F. Chu, Q. Han, *Nano Energy* **2020**, *70*, 104526.
[42] X. Shan, H. Li, Y. Yang, J. Feng, Y. Wang, T. Xie, *Energy* **2019**, *172*, 134.
[43] K. Tao, H. Yi, Y. Yang, H. Chang, J. Wu, L. Tang, Z. Yang, N. Wang, L. Hu, Y. Fu, J. Miao, W. Yuan, *Nano Energy* **2020**, *67*.
[44] S. Niu, Y. Liu, X. Chen, S. Wang, Y. S. Zhou, L. Lin, Y. Xie, Z. L. Wang, *Nano Energy* **2015**, *12*, 760.
[45] J. J. Allen, A. J. Smits, *J. Fluids Struct.* **2001**, *15*, 629.
[46] M. J. David, M. Mathur, R. N. Govardhan, J. H. Arakeri, *J. Fluid Mech.* **2018**, *839*, 489.
[47] Y. Liu, J. Liu, F.-P. Gao, *Ocean Eng.* **2023**, *269*, 113574.